Experimental investigation of airfoil turbulence-impingement noise reduction using porous treatment

Zamponi, R.; Ragni, D.; Van de Wyer, N.; Schram, C.

DOI
10.2514/6.2019-2649

Publication date
2019

Document Version
Final published version

Published in
25th AIAA/CEAS Aeroacoustics Conference, 2019

Aeroacoustics Conferences
20-23 May 2019, Delft, The Netherlands
25th AIAA/CEAS Aeroacoustics Conference

10.2514/6.2019-2649

Experimental Investigation of Airfoil Turbulence-Impingement Noise Reduction Using Porous Treatment

R. Zamponi*[1] and D. Ragni†[2] and N. Van de Wyer‡[1] and C. Schram§[1]
[1]*von Karman Institute for Fluid Dynamics, Sint-Genesius-Rode, 1640, Belgium*
[2]*Delft University of Technology, 2629 HS Delft, the Netherlands*

The present work aims at evaluating the effectiveness of the use of porous materials for reducing airfoil turbulence-impingement noise. To pursue this objective, a porous NACA-0024 profile filled with melamine foam has been designed for comparison with a solid model. The porous media constituting the airfoil has been fully characterized in order to determine the parameters that describe the material. The two profiles have been tested in a rod airfoil configuration in the anechoic chamber of von Karman Institute for Fluid Dynamics. A free-stream velocity of 30 m/s (corresponding to a chord-based Reynolds number of $3.2{\cdot}10^5$) and an angle of attack of 0° have been considered for the tests. Hot-wire anemometry measurements have been performed with the aim of characterizing the boundary layers around the two airfoils and investigating the eventual nose mitigation mechanisms that occur due to the porous treatment. Moreover, the static pressure distributions along the two surfaces have been studied to find correlations with the velocity profiles. The results show that the use of a porous treatment leads to a decrease of turbulence-impingement noise in the low-frequency range and to an increase in the high-frequency one, mostly due to surface roughness noise. The application of an inverse beamforming technique has lead to a qualitative comparison of noise distribution maps at different one-third octave band frequencies for the two cases. Furthermore, the pressure values of each map point within a rectangular region surrounding the leading edge have been summed in order to retrieve the integrated one-third octave band spectra.

Nomenclature

c	=	airfoil chord
C_p	=	pressure coefficient
CSM	=	cross-spectral matrix
d	=	cylindrical rod diameter
GIBF	=	Generalized Inverse Beamforming
JCAL	=	Johnson-Champoux-Allard-Lafarge (model)
k_0	=	viscous permeability
k_0'	=	thermal permeability
l	=	rectangular nozzle width
$\dot{m}$	=	mass flow rate
p_0	=	stagnation pressure in free-stream
p_∞	=	static pressure in free-stream
s	=	airfoil span
t	=	airfoil maximum thickness
TI	=	turbulence intensity
$\bar{u}$	=	non-dimensionalized mean velocity
u’	=	velocity fluctuations
U_∞	=	free-stream velocity

*Ph.D Candidate, Environmental and Applied Fluid Dynamics Department, riccardo.zamponi@vki.ac.be.
†Assistant Professor, Aircraft Noise & Climate Effects section, Faculty of Aerospace Engineering, d.ragni@tudelft.nl, AIAA member
‡Research Engineer, Environmental and Applied Fluid Dynamics Department, nicolas.vandewyer@vki.ac.be, AIAA member
§Associate Professor, Environmental and Applied Fluid Dynamics Department & Aeronautics and Aerospace Department, christophe.schram@vki.ac.be, AIAA member

α_∞ = tortuosity
Λ = viscous characteristic length
Λ' = thermal characteristic length
ρ = flow density
σ = static air flow resistivity
ϕ = porosity

I. Introduction

The investigation of the noise generation mechanisms involved in the interaction of a wing profile with incoming turbulence represents a core topic for applications of large societal interest, including airframe noise, aeronautical propulsion systems, HVAC systems for automotive and construction. In these instances, the turbulence is typically produced by elements such as protection grids or heat exchangers that are installed upstream of the airfoil and create inflow distortions. From the physical point of view, the sound is radiated as a consequence of the rapid changes of the turbulent vortexes inertia due to the interaction with the surface of the airfoil. Historically, the phenomenon has been studied by several authors. Paterson and Amiet [1], Migliore and Oerlemans [2] and Moreau *et al.* [3] demonstrated that turbulence-impingement noise, referred to also as leading-edge noise, is predominantly a low-frequency source when the turbulent eddies are large scale structures. Moreover, the Amiet theory [4–6] showed that the noise radiation pattern depends on the airfoil compactness with reference to the acoustic wavelength. Additional studies concerning the effect of real airfoil geometry on the interaction with a turbulent flow can be found in the work of Gill *et al.* [7, 8] and Kim *et al.* [9]. The study of the mechanism with which the turbulence-impingement noise is generated and radiated is instrumental in designing novel sound mitigation approaches. Since acting on the ingested turbulent field is often challenging, one promising strategy to reduce the turbulence-impingement noise is to make the airfoil acoustic response less sensitive to the turbulent flow. Geometrical or structural changes of the airfoil design or the usage of absorbing materials can achieve this objective.

The scope of the present work is to evaluate the effectiveness of a porous airfoil, with an impenetrable core line, in the reduction of the noise produced by turbulence impinging on its surface. The implementation of porous material as part of the structure of a wing profile has been already addressed in the past by several authors. Among them, Roger *et al.* [10, 11] filled a NACA-0012 airfoil with steel wool to investigate the leading-edge noise reduction in a grid-generated turbulent flow. In their study, the use of porous materials showed a reduction effect with a maximum of 5 dB, even though no optimization of the material parameters had been attempted. An analogous method has been adopted by Geyer *et al.* [12, 13], who tested different porous materials and different turbulence-generator grids and performed acoustic measurements on leading-edge noise using microphones array techniques. The experiments lead to a noticeable noise reduction for most of the porous profiles when compared with the non-porous cases. Similar designs for a porous airfoil have also been considered by Sarradj and Geyer [14], Geyer *et al.* [15, 16], Tinetti [17] and Herr and Reichenberg [18] in the framework of trailing edge noise mitigation. Most of the conducted studies state that the application of porous materials may have a significant potential for flow noise mitigation but also that it is necessary to improve the understanding of the influence of the porous material parameters. The previously mentioned Geyer *et al.* [12, 13] and Sarradj and Geyer [14] focused their analysis on the characterization of this influence by comparing the results of aeroacoustic wind tunnel tests on several porous and non-porous airfoils. They found that not only the overall sound pressure level, but also the spectral characteristics are dependent on the properties of the porous material, especially the static air flow resistivity. A deeper insight about these correlations should lead to a better comprehension of the physical mechanism responsible for noise reduction, since no agreement about the mode of operation of the porous treatments has been found yet, despite the numerous investigations.

This manuscript describes acoustic far-field noise and hot-wire anemometer measurements that were performed in the testing facility of von Karman Institute for Fluid Dynamics (VKI) on a NACA-0024 airfoil in a non-porous and a porous version. Specifically, melamine foam was the porous material used in these tests. A particular emphasis has been put on the characterization of the parameters of the material. The comparison between the two cases has been carried out considering one angle of attack and one flow velocity. The experimental setup consists of a rod-airfoil configuration, already used by de Santana [19]. In this arrangement, firstly proposed by Jacob *et al.* [20] as a benchmark problem for noise computation and modeling, the wing profile undergoes a broadband perturbation dominated by a preferred shedding frequency, similarly to what has been observed in most turbo-machinery applications [21]. Indeed, as stated by Roger and Moreau [11], the analysis of the turbulence-impingement noise reduction that can be achieved with the use of porous treatment provides similar results to that of a rod-airfoil and a tandem airfoil configuration.

Finally, the objective of the present effort is to demonstrate the potential benefits of this technology, rather than carrying out an in-depth investigation of its applicability. For instance, the aerodynamic performance loss that the porous airfoil may experience in comparison with the reference one that has been observed in similar works [14, 16] has not been evaluated.

II. Design and Characterization of the Porous Airfoil

The porous NACA-0024 airfoil has been designed with a chord of 0.157 m, corresponding to a maximum thickness of approximately 0.038 m, and a span of 0.200 m. The choice of this chord has been made to ease the manufacturing and instrumentation of the model. In order to avoid the cross-flow between the two sides of the profile, the core line has been made impenetrable. The volume of the airfoil has been filled with melamine foam, which is easy to cut to the desired shape. A porous hard plastic exoskeleton has the function of containing the foam and ensuring the proper shape fidelity. It is made of two components, one per each side of the airfoil surface, assembled on the solid center plane and glued in correspondence with the leading edge and the trailing edge. The same manufacturing technique has been adopted to produce the solid airfoil, whose exoskeleton does not present any porosity. All the profiles have been finally coated with the same metallic wire mesh, which protects the materials and guarantees a good quality surface roughness.

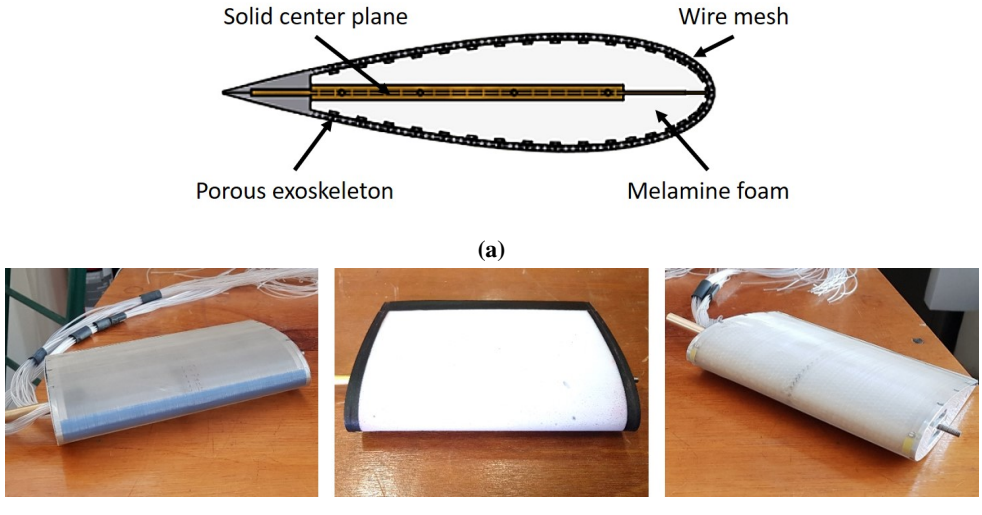

Fig. 1 (a) Representation of the porous NACA-0024 used in the experiments. (b) Comparison between the manufactured solid airfoil (on the left), the melamine airfoil (in the center) and the porous airfoil (on the right).

In Fig. 1a a representation illustrating the different parts constituting the porous airfoil is depicted. With the aim of investigating the acoustic influence of the exoskeleton and the wire mesh, a third airfoil just made of melamine foam has been created. The porous material has been cut in the shape of a NACA-0024 and glued on the solid center plane, without any other hard plastic component. Although this design does not represent a technological solution for the implementation of a porous material in the structure of the airfoil, it constitutes a basis of comparison. A photograph of the three manufactured prototypes is shown in Fig. 1b .

As mentioned above, the porous medium parameters play an important role in the investigation of noise reduction mechanisms. According to the Johnson-Champoux-Allard-Lafarge (JCAL) model, the six parameters necessary to fully characterize the material are:

- the static air flow resistivity, σ, which is described by the relationship known as Darcy's law [22] and corresponds to the ratio of a pressure difference Δp across a sample of porous material in the presence of a static fluid flow through it to the product of the flow velocity and the sample thickness;
- the porosity, ϕ, defined as the ratio between the accessible pore volume (since those pores which are closed and not accessible are not expected to have an influence on the acoustical and aerodynamical characteristics) and the total volume;
- the tortuosity, α_∞, which takes into account the sinuous fluid paths through the porous material;

- the viscous characteristic length, Λ, introduced by Johnson *et al.* [23], which considers the medium and high frequency viscous and inertial effects;
- the thermal characteristic length, Λ', defined by Champoux and Allard [24], which expresses the thermal exchanges between the material frame and the pore saturating fluid at medium and high frequencies;
- the thermal permeability, k_0', introduced by Lafarge *et al.* [25], which models the thermal exchanges between the porous material frame and the saturating fluid at low frequencies.

Besides these, another parameter that is used to define a porous medium is the viscous permeability, k_0, which is directly linked to σ. Indeed, it is defined as the ratio of the dynamic viscosity of air to the static air-flow resistivity.

The characterization of the above-mentioned quantities has been performed in collaboration with Laboratoire d'Acoustique de l'Université du Maine (LAUM). For their estimation, an inverse method based on the measurement of the melamine foam scattering matrix by means of a 4-microphone impedance tube has been considered [26]. The inversion is done in the Bayesian framework, whereas the model used for describing the porous medium is the JCAL one. The results of the characterization are listed in Table 1. The estimation is considered reliable because a good match has been found with other results from ultrasonic measurements conducted on the same sample and not discussed in this work.

Table 1 JCAL model parameters characterizing the melamine foam of the porous airfoil.

σ [Pa· s · m^{-2}]	ϕ [-]	α_∞ [-]	Λ [m]	Λ' [m]	k_0 [m^2]	k_0'[m^2]
13003.9	0.986	1.02	1.344×10^{-4}	1.942×10^{-4}	1.410×10^{-9}	2.382×10^{-9}

Concerning the parameters of the hard plastic exoskeleton and the metallic wire mesh, the first has been designed to have ϕ of 80%, whereas for the second ϕ is equal to 60.8%. Static air flow resistivity measurements have been performed at Centre de Transfert de Technologie du Mans (CTTM), in Le Mans, with samples of the two materials. As expected, the σ of the two layers was negligible, confirming the fact that the static air flow resistivity of the porous airfoil is governed by the σ of the melamine foam.

III. Experimental Set-up and Data Processing

In this section, the experimental setups and analysis tools used to carry out the aerodynamic and aeroacoustic tests are presented.

A. Rod-airfoil Configuration

The experimental facility consists of a jet installed in a semi-anechoic room with dimensions 4 m × 3 m × 4 m and a cut-off frequency of 200 Hz. A wooden circular-to-rectangular contraction, designed by de Santana [19] and characterized by an area ratio of 2.35 to 1, adapts the circular geometry of the duct to the rectangular geometry needed for the rod-airfoil configuration. The dimensions of the nozzle exit are 0.200 m for the span and 0.150 m for the width. The airfoil and the rod are held vertically by two side-plates, designed not to have sharp corners. The experimental setup with the relative distances is depicted in Fig. 2. The cylindrical rod has a diameter of 0.02 m that corresponds to the one of the leading edge circle of the airfoil. The distance between the rod axis and the leading edge is 0.174 m.

The following coordinate system is used for the description of both acoustic and hot-wire measurements: the x-axis is aligned with the jet axis and therefore with the flow direction, the y-axis is aligned with the spanwise direction of the airfoil and the z-axis is oriented in order to form a right-handed coordinate system. The origin is set in the midspan of the profile at the level of its leading edge.

All the measurements have been carried out at a 0° angle of attack of the airfoil and at a flow velocity of 30 m/s, corresponding to a chord-based Reynolds number of $3.2 \cdot 10^5$. The angle of attack and the alignment between rod and airfoil have been verified by comparing the static pressure distributions on the two sides of the airfoil.

The facility has been characterized by means of hot-wire anemometry in order to determine the mean velocity, $\bar{u}$, and the turbulence intensity, TI, profiles for different configurations. $\bar{u}$ is normalized by the flow free-stream velocity U_∞, whereas TI is defined as the ratio of the root-mean-square (r.m.s.) of the turbulent velocity fluctuations to U_∞. All the acquisitions have been performed with a single hot-wire probe connected to an in-house system and corrected in order to take into account the temperature variations during the tests. The sampling frequency has been set to 51.2 kHz, which leads to an anti-aliasing filter set to 25.6 kHz. The acquisition time for the velocity has been set at 5 s with the purpose

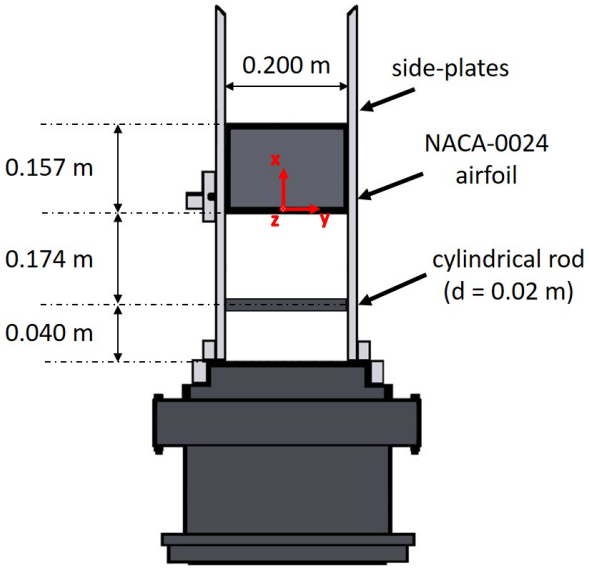

Fig. 2 Scheme of the rod-airfoil configuration installed on the cylindrical-to-rectangular contraction. The red arrows indicate the coordinate axes of the reference system.

of ensuring convergence in the results. In free-stream conditions, TI was found to be about 0.4% in the potential core of the jet at a distance of 1 mm from the nozzle exit, proving that there is almost no inflow turbulence. Figure 3 shows the $\bar{u}$ and TI profiles along the z-axis at 20 mm upstream of the leading edge and 44 mm downstream of the rod axis. In the figure, the z-axis is normalized by the width of the nozzle (l = 0.150 m). The effects of the wake of the cylindrical rod at this level consist of a 20% reduction of $\bar{u}$ and a significant increase in the value of TI, whose peak is about 30%.

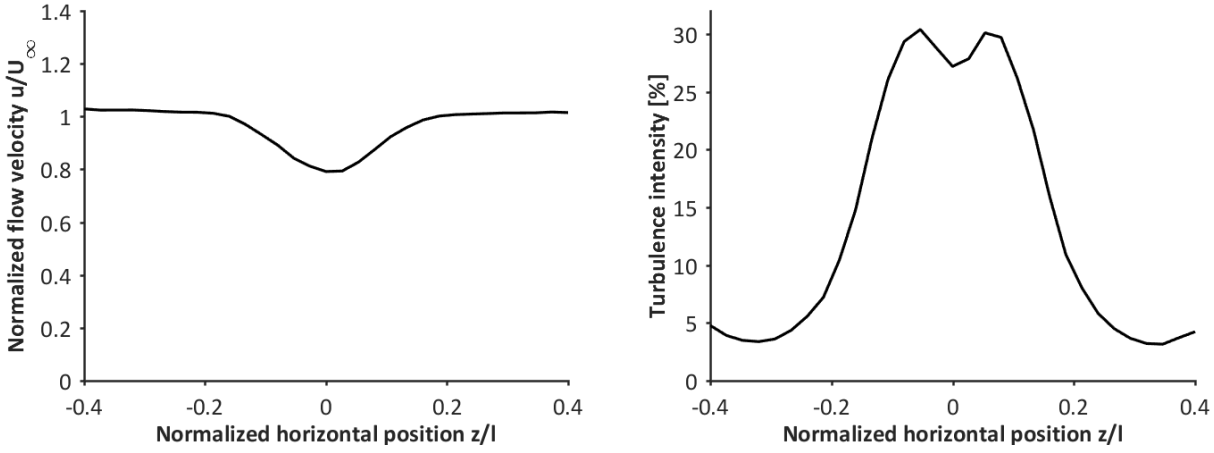

Fig. 3 Mean velocity (a) and turbulence intensity (b) profiles at 20 mm upstream of the airfoil leading edge level. l is the width of the nozzle (0.150 m).

B. Steady and Pressure Measurements

In order to perform static pressure distribution measurements, the NACA-0024 profiles have been equipped with 35 static pressure sensors. In each surface there are 17 transducers at the midspan that correspond to the 1.4%, 3.4%, 5.7%, 8.4%, 12.5%, 16.7%, 21.0%, 26.7%, 32.4%, 38.1%, 49.5%, 55.2%, 60.9%, 66.5%, 72.6% and 77.8% of the chord. An additional measurement position has been considered in correspondence with the leading edge.

The static pressure ports are connected to an in-house acquisition system that leads to the estimation of the pressure coefficient, C_p, along with the chord, defined as:

$$C_p = \frac{p - p_\infty}{p_0 - p_\infty}, \tag{1}$$

where p is the static pressure measured, p_0 is the stagnation pressure measured at the leading edge of the solid airfoil, and p_∞ is the static pressure in the free-stream. Finally, the data have been acquired at a sampling frequency of 500 Hz and with an acquisition time of 15 s.

C. Hot-Wire Measurements

The airfoil boundary layer has been characterized by means of constant temperature anemometry, with a single wire in-house system. The probe has been placed in a carriage system which allows a movement within the plane xz, at a y corresponding to the midspan of the airfoil. The wire has been oriented perpendicular to the streamwise velocity component. As in the case of the facility characterization, the sampling frequency has been set to 51.2 kHz, whereas the data have been acquired for 5 s. The first 0.5 s of acquisition have been discarded in the post-processing phase to take into account the effect of the probe vibrations during the traverse system movement. The static calibration of the hot-wire anemometer has been performed in-situ on a daily basis, using a Prandtl tube to measure the reference velocities. With the aim of taking into account the significant effect of the temperature on the measurements, an appropriate correction has been applied considering the model proposed by Bruun [27].

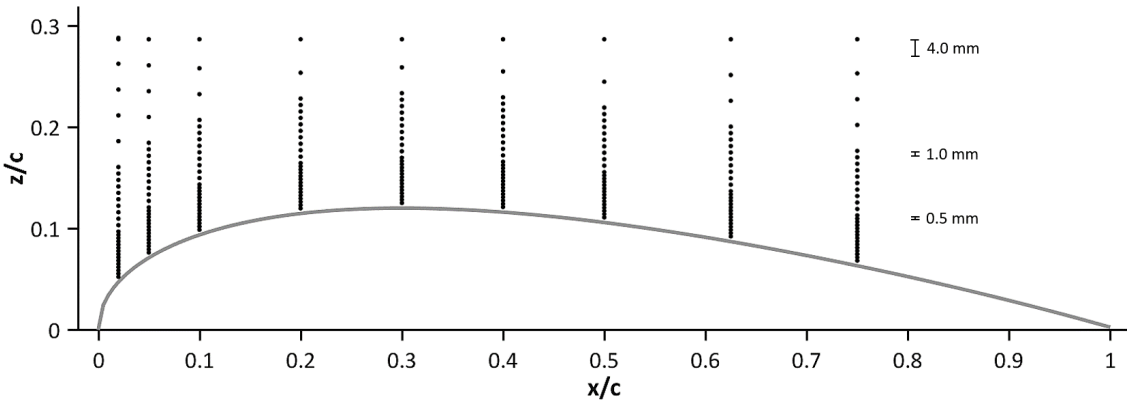

Fig. 4 Traverses for the hot-wire anemometry measurements for the characterization of the boundary layer. Nine chordwise positions are considered. Each traverse contains approximately 30 points. The y coordinate of the measurements corresponds to the airfoil midspan, inside the core jet. c is the airfoil chord (0.157 m).

Figure 4 shows the coordinates of the measurement positions which were considered for the characterization of the boundary layer. Nine chordwise coordinates have been chosen along the airfoil. As the profile is symmetric and mounted with an angle of attack of 0°, only one surface has been investigated. The x-axis positions along the airfoil correspond to the 2%, 5%, 10%, 20%, 30%, 40%, 50%, 62.5% and 75% of the chord. Approximately 30 measurement positions have been considered in the z-direction for each traverse. The distance between the points is variable and the step is 0.5 mm, 1 mm and 4 mm for respectively the first 7.5 mm, the following 10 mm and the last part. In order to avoid the contact between the wire and the metallic cloth coating the airfoil, the minimum distance of the probe from the surface has been evaluated using a dummy sensor with exactly the same geometry as the hot-wire probe. In this way, it has been possible to optically determine the exact position in which the prongs of the sensor touch the surface of the airfoil.

D. Aeroacoustic Measurements

Acoustic far-field measurements have been performed to study the eventual noise reduction achievable by the use of a porous treatment. Figure 5a shows the 64-microphones seven arms Dougherty array used for the tests. The antenna is characterized by an aperture of 1.500 m and has been placed out of the flow at 1.160 m from the airfoil. The center of the array is approximately aligned with the center of the airfoil leading edge. The microphones installed are capacitor-based

Knowles electrets. The data have been acquired with a sampling frequency of 51.2 kHz and a total of 3072000 samples per channel. The cross-spectral matrix (CSM) of the measured signals is computed by using the Welch method [28], with blocks of 8192 samples windowed using a Hann-weighting function characterized by a 50% of data overlap, thus providing a frequency resolution of 6.25 Hz. The background noise corresponding to the configuration with the rod and without the airfoil has been recorded to be taken into account during the analysis of the results.

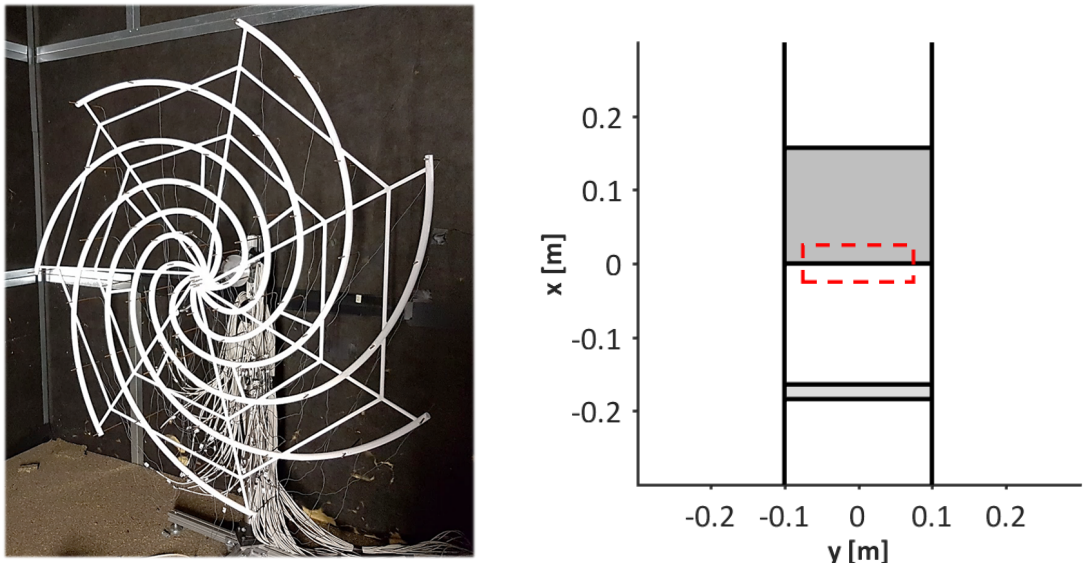

(a) (b)

Fig. 5 (a) 64 microphones seven arms Dougherty array used for acoustic measurements. (b) Source distribution map configuration. The black lines indicate side-plates, rod and airfoil leading edge and trailing edge, with the flow going from the bottom to the top of the map. The red dashed lines represent the area considered for the integrated spectra.

The data have been post-processed with a Generalized Inverse Beamforming (GIBF) technique developed at VKI and validated through its application to an experimental [29, 30] and a numerical [31] benchmark dataset. The isolation of the different noise sources that is possible to achieve with beamforming ended up being essential for the analysis of turbulence-impingement noise. In this way, the contribution of the noise coming from the open jet, of the rod self-noise and of the noise sources generated at the juncture of the side-plates and the airfoil due to the scattering of the turbulent boundary layer forming along the plates can be discarded. A similar approach has been used by Geyer *et al.* in the framework of leading-edge noise analysis for a grid-generated turbulent flow impinging on an airfoil [12, 13].

Two different analyses have been carried out using GIBF, namely, the evaluation of noise source distribution maps referred to several one-third octave band frequencies and the calculation of the corresponding one-third octave band spectra. Corrections for accounting the convection of the flow and the refraction of the shear layer have been applied, following the approach proposed by Sijtsma [32]. In addition, proper handling of the background noise plays an important role in visualizing the position of the noise sources and has been performed through an advanced subtraction method based on the eigenvalue decomposition of the measured CSM [33]. Furthermore, only the eigenmodes corresponding to the 10 most dominant eigenvalues have been computed by the algorithm to save computational time. It should be mentioned also that the source maps generated by GIBF display the source distribution contours and not the peak source intensity [34]. Therefore, the source intensity can be evaluated only after the integration procedure. This feature is useful in practice for the analysis of distributed sources and represents one of the reasons why GIBF has been chosen for the post-processing of the acoustic data. For the source maps visualization, the experimental setup is depicted as shown in Fig. 5b. The vertical black lines indicate the test section side-walls, the horizontal ones indicate rod, leading edge and trailing edge of the model. The flow goes from the bottom to the top of the map. Concerning the spectra, they are determined by summing the pressure values of each scanning grid point within a rectangular region surrounding the leading edge center. The red dashed lines in the figure indicate the integration area, whose dimension is 0.150 m $\times$ 0.050 m. The width has been chosen in order to include the noise sources eventually distributed along the leading edge

and to exclude the ones generated at the juncture with the side-plates. Finally, special care must be taken in choosing the frequency range to be analyzed. The upper limit has been set to 5 kHz, mostly due to limitations in the calibration procedure of the electret microphones. For the lower one, the constraint is normally represented by the non-compactness condition [35], which states that the considered wavelength should be smaller than the airfoil chord length for a complete separation between the noise generated at the leading edge and the one at the trailing edge. In the present case, this limit approximately corresponds to 2.15 kHz. However, the use of an advanced phased array technique such as GIBF makes it possible to separate noise sources at frequencies even below this value. The lowest one-third octave band center frequency investigated in this study is therefore 1 kHz. Below this threshold, the resolution of the map was found to be too poor to provide meaningful results due to the beamwidth characteristics of the microphone antenna.

IV. Results and Discussion

In this section, the results of the different measurements conducted at 30 m/s for a 0° angle of attack for both solid and porous airfoil are presented and discussed.

A. Static Pressure Distribution

The C_p distributions for the solid and the porous airfoil are presented in Fig. 6. These curves have been obtained by averaging the static pressure acquired on the two sides of the airfoil for each chord position. The results are compared with the prediction given by the vortex-panel method XFOIL [36]. Overall, the C_p distribution of the solid profile presents a satisfactory agreement with XFOIL, constituting a validation for the adopted measurement technique.

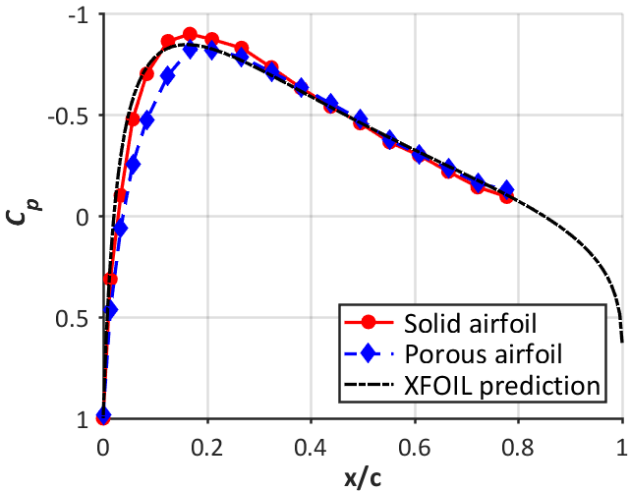

Fig. 6 C_p distribution along the airfoil chord airfoil measured for the solid and the porous airfoil and compared with the vortex-panel method XFOIL.

From the comparison of solid and porous airfoil, it is possible to observe that the minimum C_p for the two profiles in correspondence with the 17% of the chord is almost preserved. However, the porous profile reaches the peak in a more gradual way. This discrepancy is probably due to the circulation of flow through the pores of the melamine foam that is originated in the first part of the profile and tends to level out the pressure differences along its surface. Furthermore, in the second half of the airfoil, the two C_p distributions coincide. The reason for this trend is currently under investigation.

Finally, the decrease of pressure difference experienced by the porous profile may reflect a loss of lift in case of higher angles of attack. Nevertheless, as already mentioned in Section I, it is out of the scope of this paper to evaluate the aerodynamic performances of the two airfoils.

B. Boundary Layer Results

The $\bar{u}$ profiles for both airfoil configurations are presented in Fig. 7. The z-axis is normalized by the airfoil maximum thickness, t = 0.038 m. All the plots show the $\bar{u}$ profiles up to 0.678t, equivalent to about 25 mm, from the surface,

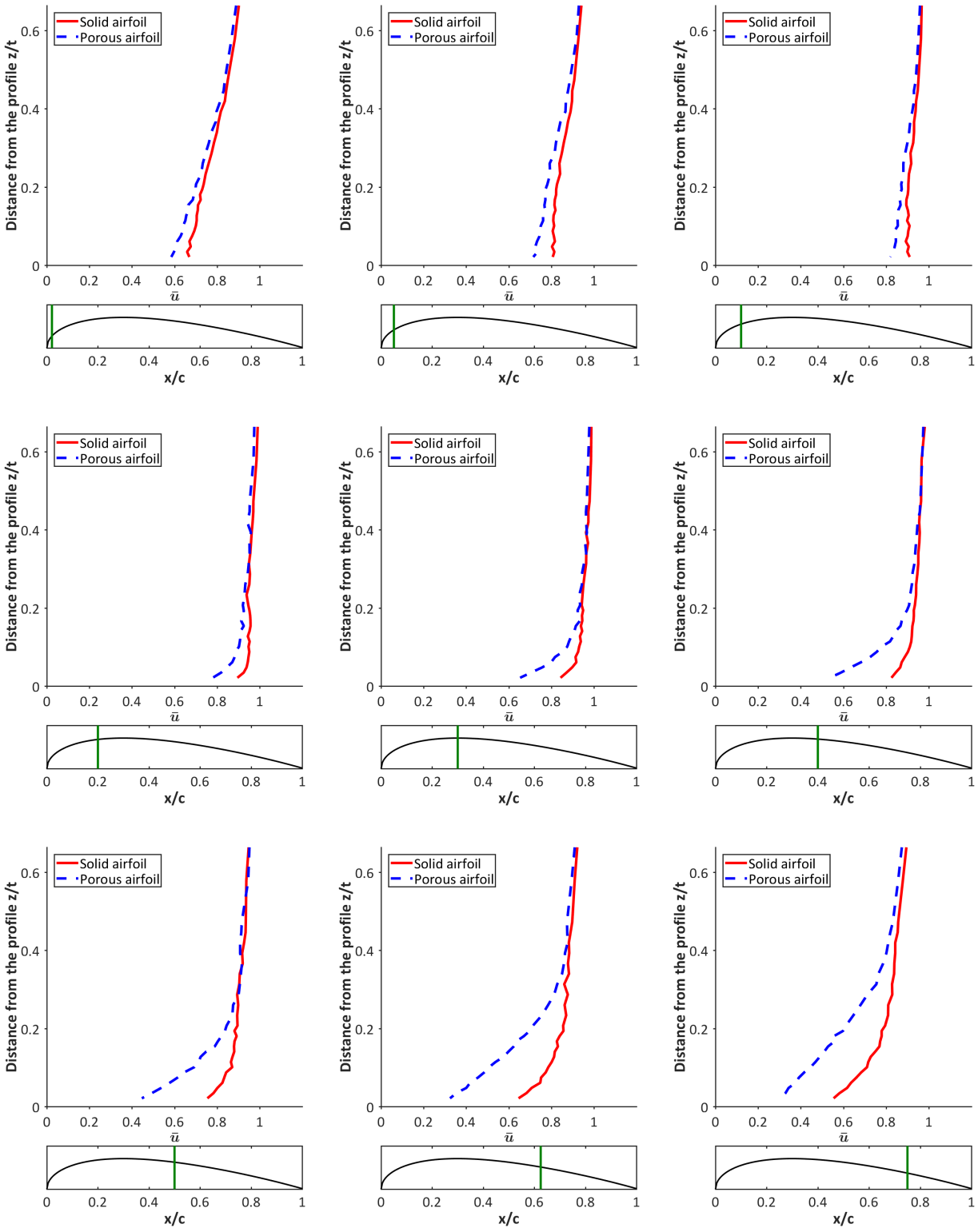

Fig. 7 Mean velocity profiles of the solid and porous airfoil for the different chordwise positions depicted in Fig. 4. t is the airfoil maximum thickness (0.038 m). The free-stream velocity is 30 m/s.

whereas the minimum distance between the hot-wire probe and the airfoil is variable and ranges from 0.5 mm to 0.8 mm. Before proceeding with a discussion of the results, it is important to point out that the profiles for the first three traverses (2%, 5% and 10%) of both solid and porous cases do not present the typical trend of the turbulent boundary layer over a flat plate. This divergence is due to the fact that the considered traverses are not perpendicular to the airfoil surface, making it difficult to relate the measured $\bar{u}$ profile to a *standard* one.

The comparison shows that the $\bar{u}$ distribution is generally lower in the boundary layer of the porous case with regard to the solid one. The origin of this mass flow deficiency is probably linked to the possibility that part of the incident velocity could penetrate the melamine foam, generating a flow circulation within the pores of the porous medium. Particularly, the decrease of mean velocity for the porous airfoil in the initial region of the profile may be related to better hydrodynamic absorption of the turbulent vortical structures generated by the rod. This phenomenon is seen as one of the possible mechanisms responsible for turbulence-impingement noise reduction [11].

In order to quantify the velocity loss experienced by the porous airfoil, the mass flow rate $\dot{m}$ has been evaluated by integrating the velocity profiles within a rectangular region, as expressed in:

$$\dot{m} = \rho s \int_{z_l}^{z_u} u(z) dz, \tag{2}$$

where ρ is the flow density, s is the airfoil span (200 mm) and z_l and z_u define the extension of the integration area. Specifically, for each traverse z_l corresponds to the point closest to the airfoil surface, whereas z_u amounts to z_l + 25 mm. The integration has been implemented using the trapezoidal rule. The results of the calculation are shown in Figure 8.

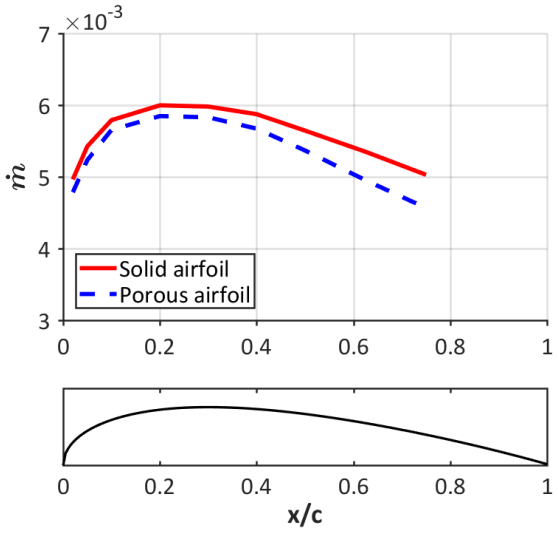

Fig. 8 Mass flow rate for the solid and porous airfoil computed with Equation 2.

Interestingly, as it is possible to observe, the magnitude of mass flow loss which is due to the presence of the porous medium increases with the increasing chordwise position, reaching a maximum $\Delta\dot{m}$ of about 10% for x/c = 0.75. This particular trend has also been observed by Geyer *et al.* [15] in the framework of trailing-edge noise reduction. In that case, results showed that the magnitude of velocity deficiency was linked to the parameters of the employed porous material. Specifically, the lower the static air flow resistivity of the porous medium, the greater the mass flow loss within the profile boundary layer.

Finally, the TI profiles for both airfoil configurations are presented in Fig. 9. The results show that in the initial part of the profile reduction of TI occurs in the proximity of the surface due to the porous treatment. The decrease of the r.m.s. velocity fluctuations may be correlated to a less efficient turbulence-impingement noise generation mechanism. However, the discrepancy in the TI profiles of the porous case with respect to the solid one reduces with the increasing chordwise position. At x/c = 20%, the two curves almost coincide. Curiously, this trend reflects the one observed in the C_p distribution shown in Fig. 6. Further investigation will shed light on eventual correlations between these physical quantities. For x/c > 20%, a trend inversion has been reported, with the TI profile for the porous configuration overcoming the TI profile for the solid one within the boundary layer. In these circumstances, the magnitude of the

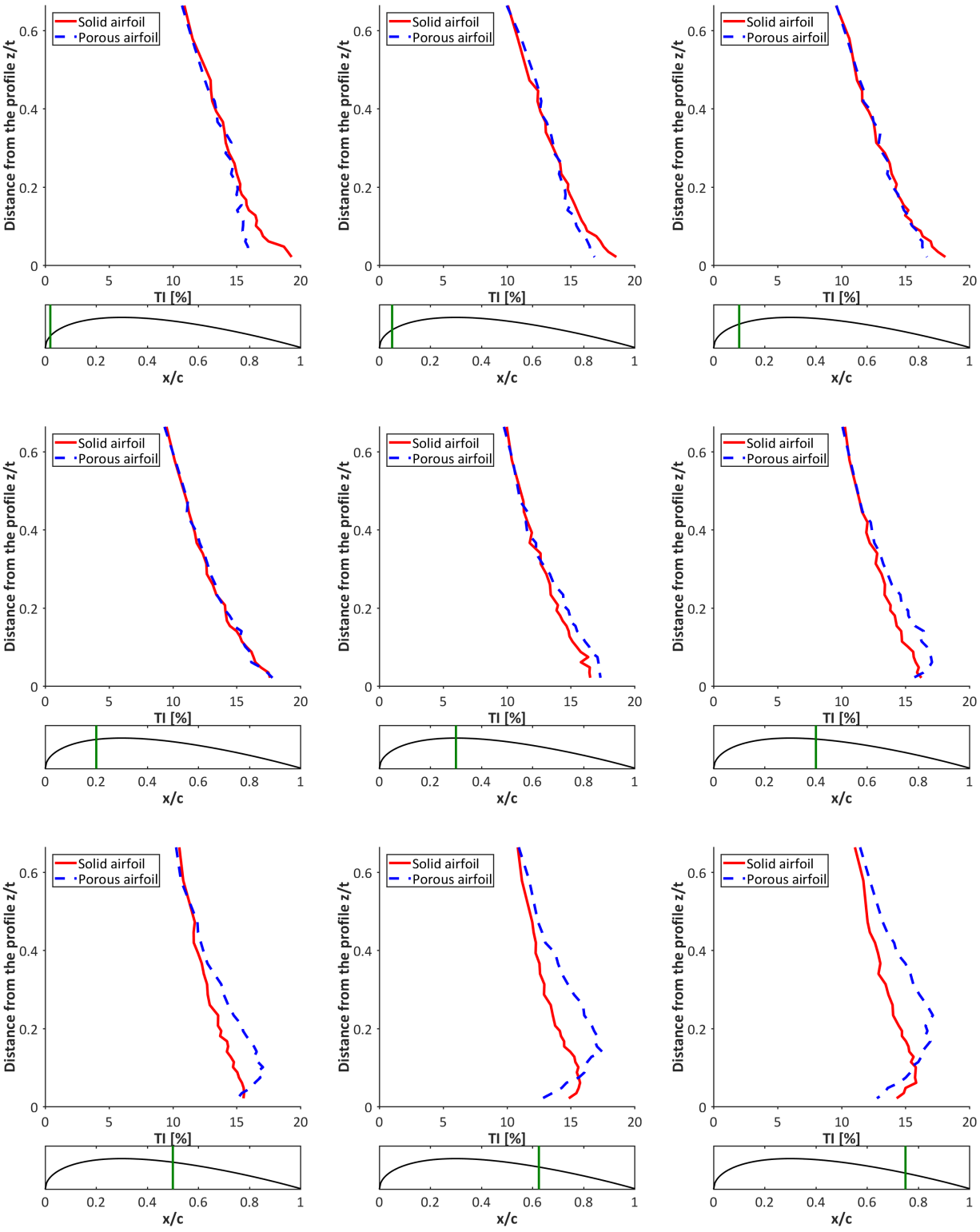

Fig. 9 Turbulence intensity profiles of the solid and porous airfoil for the different chordwise positions depicted in Fig. 4. t is the airfoil maximum thickness (0.038 m). The free-stream velocity is 30 m/s.

discrepancy increases with the increasing chordwise direction. Moreover, for x/c > 40%, the hump of the TI profile for the porous configuration moves away from the airfoil surface and the TI peak occurs at higher z/t. The increment of r.m.s. velocity fluctuations that the flow experiences for high x/c might also be linked to the afore-mentioned circulation of flow generated in the first part of the airfoil and partially blowing in the second part from the pores of the melamine foam. Indeed, the presence of a steady cross-flow blowing within the measurement location has been proved to increase the TI within the boundary layer, as stated by Kametani *et al.* [37]. Nevertheless, future tests will be necessary to fully understand the nature of this phenomenon and to confirm the assumptions made.

C. Aeroacoustic Results

In this section, the qualitative one-third octave band source maps and the quantitative one-third octave band spectra are presented.

1. One-third octave band source maps

The noise source maps related to the one-third octave band center frequency of 1.25 kHz, 2.5 kHz, 3.15 kHz and 5 kHz for both solid and porous airfoil are shown and compared respectively in Fig. 10 to 13. The spatial resolution of each map is 20 mm, whereas the dynamic range is set to 20 dB and it is the same for the two cases. In the results shown, the facility background noise has been already subtracted for more clear visualization of the noise sources. This procedure is more effective the more incoherent the background noise is with respect to the investigated sources since the subtraction method is based on the eigenvalue decomposition of the measured CSM*. In addition, a Gaussian filter has been exploited with the purpose of improving the readability of the maps.

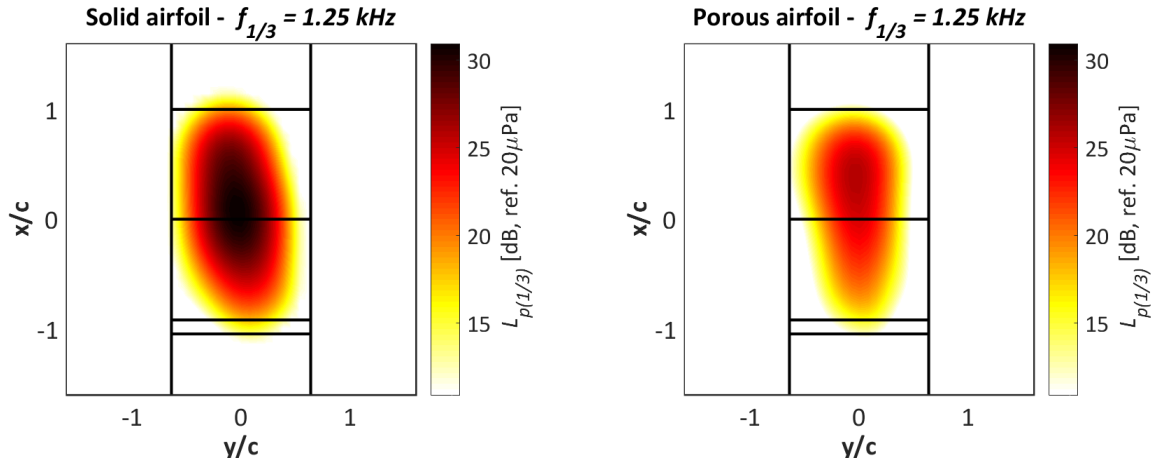

Fig. 10 Noise source distribution maps for the solid (on the left) and porous (on the right) airfoil processed with GIBF at a $f_{1/3}$ of 1.25 kHz. The dynamic range of the maps is set to 20 dB for both cases. An advanced background subtraction technique [33] has been applied in order to reduce the contribution of the rod noise.

In general, in all sound maps the main noise sources are located at the airfoil leading edge and this is most probably due to the impingement with the turbulent flow generated by the rod. At $f_{1/3}$ = 1.25 kHz (Fig. 10), the porous airfoil effectively reduces noise. Indeed, as it is possible to see in the map, the source intensity levels surrounding the leading edge area are lower than the ones of the solid airfoil. However, due to the frequency-dependent beamwidth characteristics of the antenna, the resolution of the localization is limited and it is not possible to observe the expected distributed nature of the source. At $f_{1/3}$ = 2.5 kHz (Fig. 11), the porous treatment of the airfoil is not effective anymore and an increase instead of a reduction of turbulence-impingement noise is noticed. For the solid case, the main source intensity contours are distributed along the leading edge and in correspondence with the rod. At this range of frequencies, the subtraction method is not able to fully suppress the contribution of the rod self-noise, which is dominant. This may also be due to a partial coherence between turbulence-impingement noise and the trailing edge noise of the rod. In addition, the presence of a noise source can be seen also at the trailing edge of the airfoil. For the porous case, three main peaks

*Each eigenmode of the decomposed CSM is linked to a coherent source distribution under constraint of orthogonality [34].

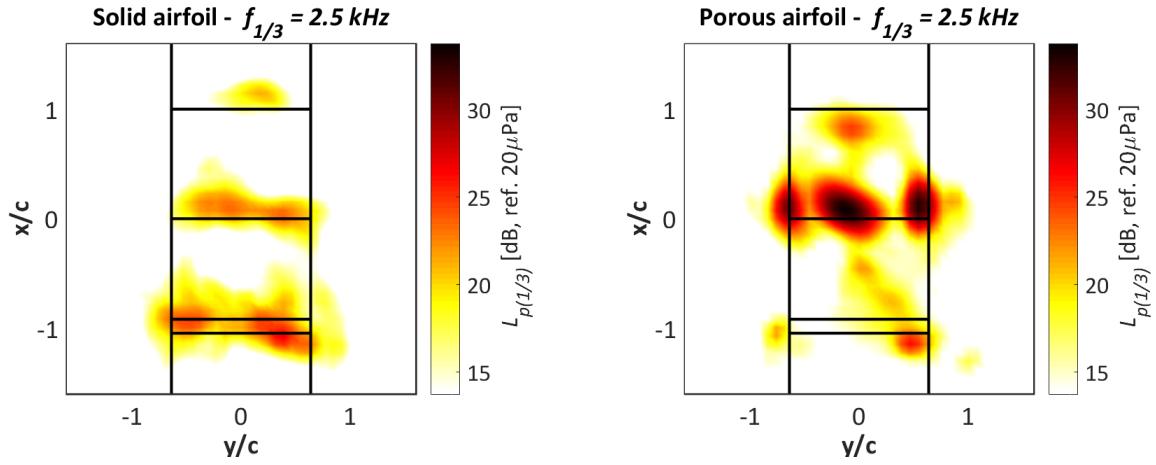

Fig. 11 Noise source distribution maps for the solid (on the left) and porous (on the right) airfoil processed with GIBF at a $f_{1/3}$ of 2.5 kHz. The dynamic range of the maps is set to 20 dB for both cases. An advanced background subtraction technique [33] has been applied in order to reduce the contribution of the rod noise.

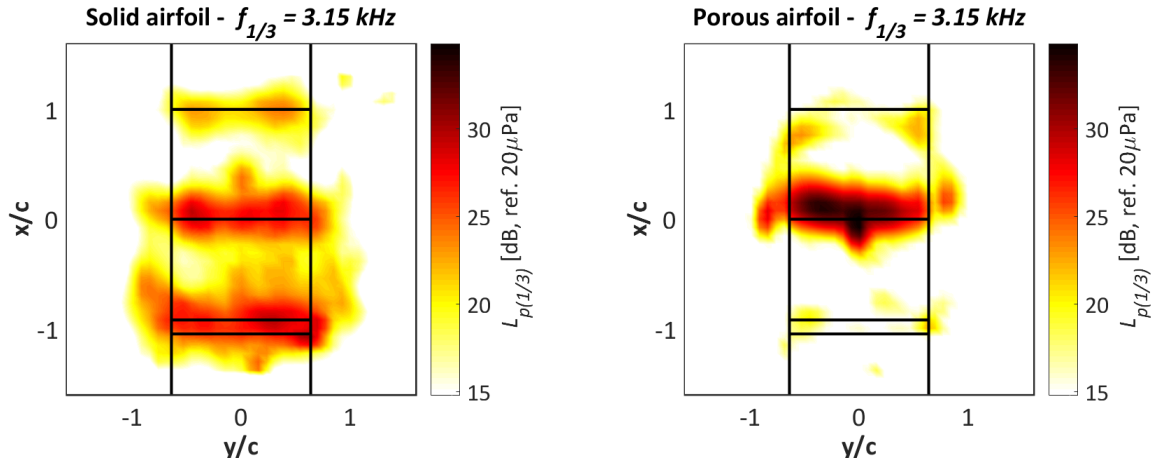

Fig. 12 Noise source distribution maps for the solid (on the left) and porous (on the right) airfoil processed with GIBF at a $f_{1/3}$ of 3.15 kHz. The dynamic range of the maps is set to 20 dB for both cases. An advanced background subtraction technique [33] has been applied in order to reduce the contribution of the rod noise.

are present at the leading edge, one at the midspan and two in the proximity of the juncture with the side-plates. The reason for the detected noise increase could be related to higher surface roughness, given by the melamine foam and by the pores of the hard plastic exoskeleton. The choice of the wire mesh, common to both airfoils, might also influence the noise reduction. A deeper investigation will be required for a better understanding of these phenomena. A similar trend can be observed also at $f_{1/3}$ = 3.15 kHz (Fig. 12). In this case, the localization accuracy improves with the increasing frequency and it is possible to detect the distributed nature of the leading-edge noise. For the solid airfoil, the main source intensity peaks are still located along the rod, whereas the porous one presents the same two peaks in the vicinity of the side-plates already discussed before. In addition, also the contribution of the turbulent boundary layer scattering at the trailing edge is visible in the map for the solid airfoil. At $f_{1/3}$ = 5 kHz (Fig. 13), the noise increase due to the presence of the melamine foam still appears to be significant. Moreover, the analysis at this frequency shows an interesting aspect concerning the position of the source region. Particularly, in the solid airfoil, the main source intensity peaks are distributed exactly along the leading edge, whereas in the porous one their position is slightly shifted downstream. This may indicate a different noise generation mechanism linked to the circulation of flow through the pores of the porous medium. The investigation of the related phenomenon can bring light to the effective operating principle of porous materials in the framework of turbulence-impingement noise reduction.

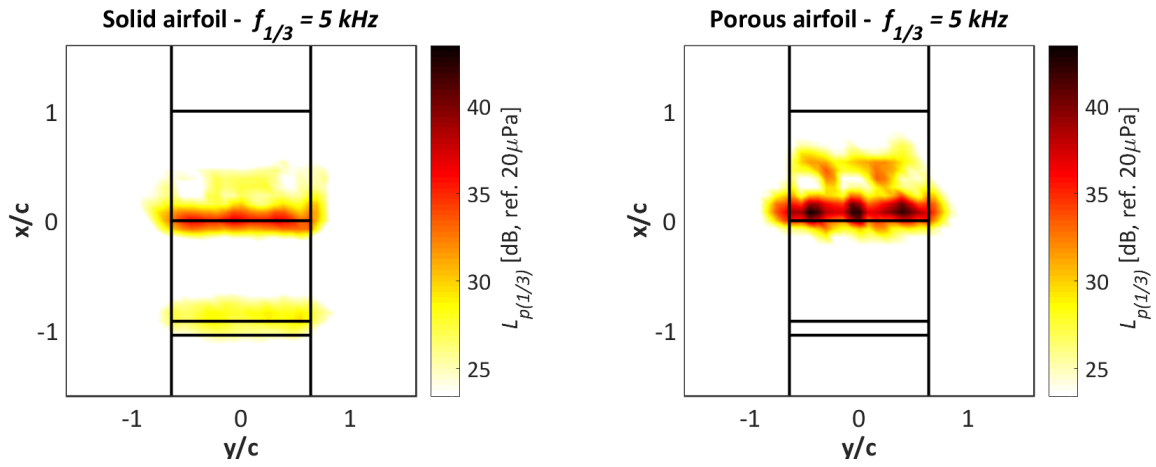

Fig. 13 Noise source distribution maps for the solid (on the left) and porous (on the right) airfoil processed with GIBF at a $f_{1/3}$ of 5 kHz. The dynamic range of the maps is set to 20 dB for both cases. An advanced background subtraction technique [33] has been applied in order to reduce the contribution of the rod noise.

2. One-third octave band spectra

The GIBF integrated one-third octave band spectra referred to the center of the array for one-third octave band frequency centers ranging from 1 kHz to 5 kHz are shown in Fig. 14a. The performances of the solid and the porous airfoil are compared with the ones of the profile just made of melamine foam, already mentioned in Section II and referred to as "melamine airfoil". For a better representation of the noise reduction given by the porous treatment, in Fig. 14b the difference between the one-third octave sound pressure level, $L_{p(1/3)}$, between the solid and the porous case and between the solid and the melamine case is shown.

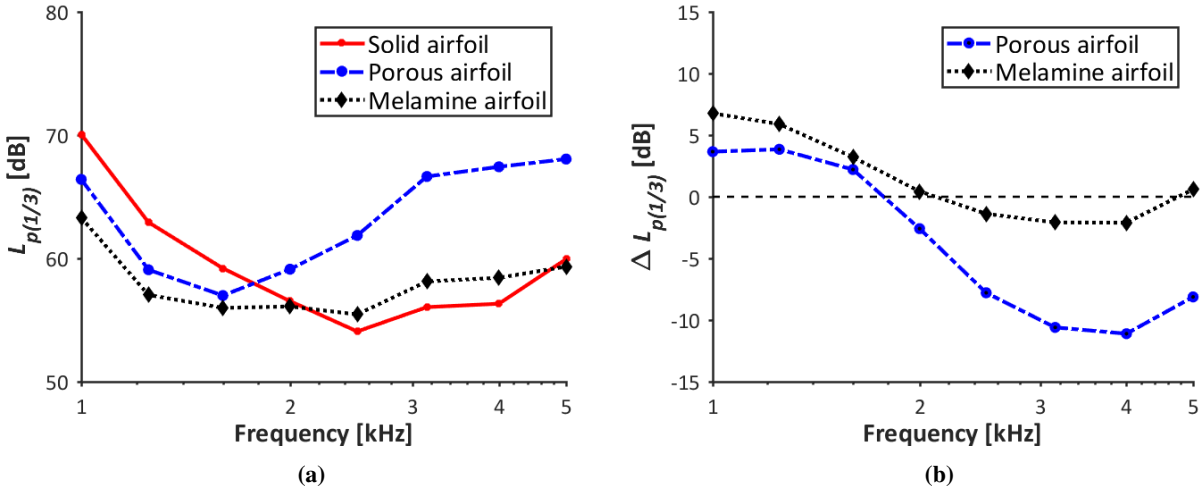

Fig. 14 (a) Integrated one-third octave band spectra processed by GIBF considering a rectangular region surrounding the leading edge and referred to the one-third octave band frequency centers ranging from 1 kHz to 5 kHz. The solid airfoil (in red), the porous airfoil (in blue) and the melamine airfoil (in black) are investigated. (b) Relative noise reduction due to the porous treatment of the airfoil with respect to the solid case. The black dashed line indicates the boundary between reduction and increase of noise.

As can be noticed, the trend of noise reduction follows what has been already qualitatively observed with the GIBF source maps. For frequencies up to almost 2 kHz, the porous treatment is effective and turbulence-impingement noise turns out to be mitigated, with a maximum reduction of about 4 dB that may be linked to the hydrodynamic absorption

given by the porous medium that has been discussed in the previous section. Above the already mentioned threshold, the surface roughness noise becomes dominant and the noise increases, reaching a maximum value of almost 12 dB at 4 kHz. Concerning the melamine airfoil, it performs better than the porous one, as could have been expected. Up to 1.6 kHz, the one-third octave sound pressure level of the two profiles follows the same trend, with a maximum scattering of about 2 dB. However, above 1.6 kHz, they start diverging, reaching a maximum $\Delta L_{P(1/3)}$ of 8 dB, and this affects also the cross-over frequency with the solid airfoil, which is at 2.1 kHz. Once this value is overcome, also the melamine case is found to be noisier than the solid case, mostly due to the increment of surface roughness noise. Anyway, the increase is significantly lower than the one for the porous airfoil, suggesting that the hard plastic exoskeleton has a drastic impact in $L_{P(1/3)}$ at high frequencies. The physical mechanism behind this phenomenon is still under investigation. Concerning the effect of the wire mesh, it contributes to the surface roughness noise, but since the same grid has been applied to both profiles its influence does not affect the reduction. New wire meshes will be tested in future studies.

One possible way to improve the noise mitigation process can be the implementation of a different porous material in the exoskeleton. In the studies conducted by Geyer *et al.* [12, 13], they stated that the materials able to grant the highest turbulence-impingement noise reduction were those with a low static air flow resistivity. According to them, it can be assumed that this effect is caused by the larger pores that characterize them. In these regards, the use of polyurethane foams represents a promising solution that can be applied in the proposed design.

V. Conclusion

The results of various tests have been presented in this paper to evaluate the effectiveness of the use of melamine foam as part of the structure of a wing profile for the reduction of turbulence-impingement noise on a NACA-0024 in a rod-airfoil configuration. Specifically, hot-wire anemometry, static pressure distributions and beamforming measurements have been performed. The outcomes of the hot-wire tests show that the boundary layer around the airfoil is affected by the presence of the porous medium, resulting in a lower mean velocity distribution in the proximity of the porous surface if compared with the solid one. The analysis showed also that the root-mean-square velocity fluctuations in the initial part of the profile are reduced due to the porous treatment. Moreover, the static pressure distribution measured on the airfoil surface is influenced by the circulation of flow through the pores of the porous medium, that tends to level out the pressure differences. Concerning the acoustic measurements, inverse beamforming is able to properly isolate the leading-edge noise due to impingement with the rod-generated turbulence. The source intensity strength is evaluated by integrating the source distribution maps within a rectangular region surrounding the airfoil leading edge. The comparison between the one-third octave integrated spectra shows that for frequencies up to almost 2 kHz the turbulence-impingement noise is effectively reduced, with a promising maximum reduction of about 4 dB. The noise mitigation in the low-frequency regime may be connected to the hydrodynamic absorption of part of the incident velocity through the porous medium, phenomenon confirmed by hot-wire and static pressure distribution measurements. Above 2 kHz, the surface roughness noise of the porous treatment overcomes the surface roughness noise of the solid profile, reaching a maximum value of almost 12 dB. Furthermore, the noise increase at high frequencies is also significantly affected by the way the porous material is implemented in the airfoil, as the use of a third profile made solely from melamine foam has shown.

Further studies will be necessary to fully understand the operating principle of porous materials in the noise reduction mechanism. In particular, the relationship between hydrodynamic absorption and noise mitigation needs to be deeply investigated. Finally, new porous materials characterized by different properties will be tested with the proposed design in order to extend the analysis and to optimize the turbulence-impingement noise reduction.

Acknowledgments

This project has received funding from the European Union's Horizon 2020 research and innovation programme under the Marie Skłodowska-Curie grant agreement No. 722401. The work is also part of the IMAGE project (Innovative Methodologies and technologies for reducing Aircraft noise Generation and Emission), which is a EU-China collaborative project, funded, for EU partners, by the European Community in the H2020 programme under Contract No. 688971-IMAGE and, for Chinese participants, by the MIIT of China.

References

[1] Paterson, R., and Amiet, R., "Acoustic radiation and surface pressure characteristics of an airfoil due to incident turbulence," *3rd Aeroacoustics Conference*, American Institute of Aeronautics and Astronautics, Palo Alto,CA,U.S.A., 1976.

[2] Migliore, P., and Oerlemans, S., "Wind Tunnel Aeroacoustic Tests of Six Airfoils for Use on Small Wind Turbines*," *Journal of Solar Energy Engineering*, Vol. 126, No. 4, 2004, pp. 974–985.

[3] Moreau, S., and Roger, M., "Effect of Angle of Attack and Airfoil Shape on Turbulence-Interaction Noise," *11th AIAA/CEAS Aeroacoustics Conference*, Aeroacoustics Conferences, American Institute of Aeronautics and Astronautics, 2005.

[4] Amiet, R. K., "Acoustic radiation from an airfoil in a turbulent stream," *Journal of Sound and Vibration*, Vol. 41, No. 4, 1975, pp. 407–420.

[5] Amiet, R. K., "High frequency thin-airfoil theory for subsonic flow," *AIAA Journal*, Vol. 14, No. 8, 1976, pp. 1076–1082.

[6] Amiet, R. K., "Noise due to turbulent flow past a trailing edge," *Journal of Sound and Vibration*, Vol. 47, No. 3, 1976, pp. 387–393.

[7] Gill, J., Zhang, X., and Joseph, P., "Symmetric airfoil geometry effects on leading edge noise," *The Journal of the Acoustical Society of America*, Vol. 134, No. 4, 2013, pp. 2669–2680.

[8] Gill, J. R., Zhang, X., and Joseph, P., "Effects of Real Airfoil Geometry on Leading Edge Gust Interaction Noise," *19th AIAA/CEAS Aeroacoustics Conference*, American Institute of Aeronautics and Astronautics, Berlin, Germany, 2013.

[9] Kim, D., Lee, G.-S., and Cheong, C., "Inflow broadband noise from an isolated symmetric airfoil interacting with incident turbulence," *Journal of Fluids and Structures*, Vol. 55, 2015, pp. 428–450.

[10] Roger, M., Schram, C., and De Santana, L., "Reduction of Airfoil Turbulence-Impingement Noise by Means of Leading-Edge Serrations and/or Porous Material," *19th AIAA/CEAS Aeroacoustics Conference*, American Institute of Aeronautics and Astronautics, Berlin, Germany, 2013.

[11] Roger, M., and Moreau, S., "Airfoil Turbulence-Impingement Noise Reduction by Porosity or Wavy Leading-Edge Cut: Experimental Investigations," *InterNoise16*, INTER-NOISE and NOISE-CON Congress and Conference Proceedings, Hamburg, DE, 2016, pp. 5848–6840, pp. 6366–6375(10).

[12] Geyer, T., Sarradj, E., Giesler, J., and Hobracht, M., "Experimental assessment of the noise generated at the leading edge of porous airfoils using microphone array techniques," *17th AIAA/CEAS Aeroacoustics Conference (32nd AIAA Aeroacoustics Conference)*, American Institute of Aeronautics and Astronautics, Portland, Oregon, 2011.

[13] Geyer, T., Sarradj, E., and Giesler, J., "Application of a Beamforming Technique to the Measurement of Airfoil Leading Edge Noise," *Advances in Acoustics and Vibration*, Vol. 2012, 2012, pp. 1–16.

[14] Sarradj, E., and Geyer, T., "Noise Generation by Porous Airfoils," *13th AIAA/CEAS Aeroacoustics Conference (28th AIAA Aeroacoustics Conference)*, American Institute of Aeronautics and Astronautics, Rome, Italy, 2007.

[15] Geyer, T., Sarradj, E., and Fritzsche, C., "Porous Airfoils: Noise Reduction and Boundary Layer Effects," *International Journal of Aeroacoustics*, Vol. 9, No. 6, 2010, pp. 787–820.

[16] Geyer, T., Sarradj, E., and Fritzsche, C., "Measurement of the noise generation at the trailing edge of porous airfoils," *Experiments in Fluids*, Vol. 48, No. 2, 2010, pp. 291–308.

[17] Tinetti, A. F., "On the Use of Surface Porosity to Reduce Wake-Stator Interaction Noise," Ph.D. thesis, Virginia Tech, Sep. 2001.

[18] Herr, M., and Reichenberger, J., "In Search of Airworthy Trailing-Edge Noise Reduction Means," *17th AIAA/CEAS Aeroacoustics Conference (32nd AIAA Aeroacoustics Conference)*, American Institute of Aeronautics and Astronautics, Portland, Oregon, 2011.

[19] de Santana, L. D., "Semi-analytical methodologies for airfoil noise prediction," Ph.D. thesis, KU Leuven, 2015.

[20] Jacob, M. C., Boudet, J., Casalino, D., and Michard, M., "A rod-airfoil experiment as a benchmark for broadband noise modeling," *Theoretical and Computational Fluid Dynamics*, Vol. 19, No. 3, 2005, pp. 171–196.

[21] Lorenzoni, V., Tuinstra, M., and Scarano, F., "On the use of time-resolved particle image velocimetry for the investigation of rod–airfoil aeroacoustics," *Journal of Sound and Vibration*, Vol. 331, No. 23, 2012, pp. 5012–5027.

[22] Scheidegger, A., *The Physics of Flow Through Porous Media*, University of Toronto Press, 1963.

[23] Johnson, D. L., Koplik, J., and Dashen, R., "Theory of dynamic permeability and tortuosity in fluid-saturated porous media," *Journal of Fluid Mechanics*, Vol. 176, 1987, pp. 379–402.

[24] Champoux, Y., and Allard, J., "Dynamic tortuosity and bulk modulus in air-saturated porous media," *Journal of Applied Physics*, Vol. 70, No. 4, 1991, pp. 1975–1979.

[25] Lafarge, D., Lemarinier, P., Allard, J. F., and Tarnow, V., "Dynamic compressibility of air in porous structures at audible frequencies," *The Journal of the Acoustical Society of America*, Vol. 102, No. 4, 1997, pp. 1995–2006.

[26] Niskanen, M., Groby, J.-P., Duclos, A., Dazel, O., Le Roux, J. C., Poulain, N., Huttunen, T., and Lähivaara, T., "Deterministic and statistical characterization of rigid frame porous materials from impedance tube measurements," *The Journal of the Acoustical Society of America*, Vol. 142, No. 4, 2017, pp. 2407–2418.

[27] Bruun, H. H., "Hot-Wire Anemometry: Principles and Signal Analysis," *Measurement Science and Technology*, Vol. 7, No. 10, 1996.

[28] Welch, P., "The use of fast Fourier transform for the estimation of power spectra: A method based on time averaging over short, modified periodograms," *IEEE Transactions on Audio and Electroacoustics*, Vol. 15, No. 2, 1967, pp. 70–73.

[29] Zamponi, R., de Wyer, N. V., and Schram, C., "An Improved Regularization of the Generalized Inverse Beamforming Applied to a Benchmark Database," *7th Berlin Beamforming Conference*, BeBeC, Berlin, DE, 2018.

[30] Zamponi, R., Van de Wyer, N., and Schram, C. F., "Benchmark Assessment of an Improved Regularization Technique for Generalized Inverse Beamforming," *2018 AIAA/CEAS Aeroacoustics Conference*, American Institute of Aeronautics and Astronautics, Atlanta, Georgia, 2018.

[31] Merino-Martinez, R., Sijtsma, P., Rubio Carpio, A., Zamponi, R., Luesutthiviboon, S., Malgoezar, A. M. N., Snellen, M., Van de Wyer, N., Schram, C., and Simons, D. G., "Integration methods for distributed sound sources," *International Journal of Aeroacoustics*, 2018. Accepted for publication.

[32] Sijtsma, P., "Phased Array Beamforming Applied to Wind Tunnel And Fly-Over Tests," Tech. rep., National Aerospace Laboratory NLR, Oct. 2010.

[33] Bahr, C. J., and Horne, W. C., "Advanced Background Subtraction Applied to Aeroacoustic Wind Tunnel Testing," *21st AIAA/CEAS Aeroacoustics Conference*, American Institute of Aeronautics and Astronautics, Dallas, TX, 2015.

[34] Suzuki, T., "L1 generalized inverse beam-forming algorithm resolving coherent/incoherent, distributed and multipole sources," *Journal of Sound and Vibration*, Vol. 330, No. 24, 2011, pp. 5835–5851.

[35] Blake, W. K., *Mechanics of Flow-Induced Sound and Vibration, Volume II: Complex Flow-Structure Interactions*, 2nd ed., Academic Press, 2017.

[36] Drela, M., "XFOIL: An Analysis and Design System for Low Reynolds Number Airfoils," *Low Reynolds Number Aerodynamics*, edited by T. J. Mueller, Springer Berlin Heidelberg, 1989, pp. 1–12.

[37] Kametani, Y., Fukagata, K., Örlü, R., and Schlatter, P., "Effect of uniform blowing/suction in a turbulent boundary layer at moderate Reynolds number," *International Journal of Heat and Fluid Flow*, Vol. 55, 2015, pp. 132–142.